

# We are IntechOpen, the world's leading publisher of Open Access books Built by scientists, for scientists

6,900

Open access books available

185,000

International authors and editors

200M

Downloads

Our authors are among the

154

Countries delivered to

TOP 1%

most cited scientists

12.2%

Contributors from top 500 universities



WEB OF SCIENCE™

Selection of our books indexed in the Book Citation Index  
in Web of Science™ Core Collection (BKCI)

Interested in publishing with us?  
Contact [book.department@intechopen.com](mailto:book.department@intechopen.com)

Numbers displayed above are based on latest data collected.  
For more information visit [www.intechopen.com](http://www.intechopen.com)



---

# Optimization of Third Generation Nanostructured Silicon-Based Solar Cells

---

Foozieh Sohrabi, Arash Nikniazi and Hossein Movla

Additional information is available at the end of the chapter

<http://dx.doi.org/10.5772/51616>

---

## 1. Introduction

Recently, the demand of solar cells has rapidly been growing with an increasing social interest in photovoltaic energy. Improving the energy conversion efficiency of solar cells by developing the technology and concepts must be increasingly extended as one of the key components in our future global energy supplement, but, the main problem of photovoltaic modules are their rather high production and energy cost.

Third generation solar cell is an alternative type of the promising device, which aims to achieve high-efficiency devices with low cost in comparison with expensive first generation solar cells and low-efficiency second generation solar cells. One of the prominent types is Si-based third generation solar cells which benefit from thin film processes and abundant, nontoxic materials. To gain efficiencies more than Shockley and Queisser limit which states the theoretical upper limit of 30% for a standard solar cell and overcome the loss mechanisms in this generation, different methods have been proposed:

1. Utilization of materials or cell structures incorporating several band gaps:
  - Si-based multi-junction solar cells
2. Modification of the photonic energy distribution prior to absorption in a solar cell:
  - Photon energy down-conversion
  - Photon energy up-conversion
3. Reducing losses due to thermalization:
  - Hot carrier solar cells
  - Impact ionization solar cells

This chapter mainly brings out an overview of the optimization of the first strategy and briefly the second and third strategies accompanying nanostructures. Multijunction solar cells are stacks of individual solar cells with different energy threshold each absorbing a different band of the solar spectrum. Si-based tandems based on quantum dots (QDs) and quantum wires (SiNWs) allowing band gap engineering and their optimization methods influencing their optical and electrical properties such as suitable Si QDs and SiNWs fabrication methods in various matrixes, interconnection between QDs, optimized impurity doping, etc. will be discussed. Moreover, the effects of the spacing and the size of Si QDs and SiNWs and their efficient amounts considering the latest researches will be introduced.

Another important process is multiple exciton generation (MEG) in QDs due to the current scientific interest in efficient formation of more than one photoinduced electron-hole pair upon the absorption of a single photon for improving solar devices.

Afterwards, the structural and superficial effects on the optimization of Si-based third generation solar cell like light concentration and use of forming gas will be presented.

Finally, the outlook concerning the mentioned methods will be suggested.

## 2. Principle of third generation solar cells based on silicon

The main aim of third generation solar cell is obtaining high efficiency. To achieve such efficiency improvements, devices aim to circumvent the Shockley-Queisser limit for single-bandgap devices that limits efficiencies to either 31% or 41%, depending on concentration ratio (Fig. 1).

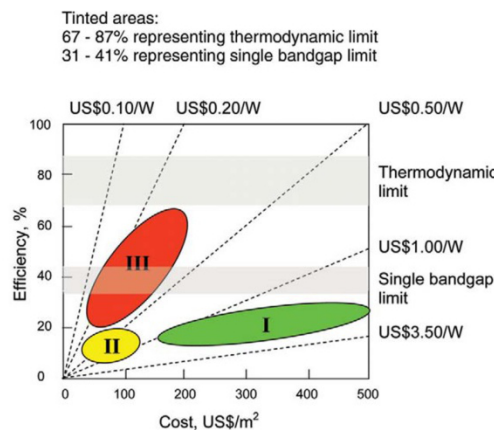


**Figure 1.** Efficiency and cost projections for first- (I), second- (II), and thirdgeneration (III) PV technologies (wafer-based, thin films, and advanced thin films, respectively) [2].

The two most important power-loss mechanisms in single band gap cells are the inability to absorb photons with energy less than the bandgap (1 in Fig. 2) and thermalization of photon energies exceeding the bandgap in which the excess energy is lost as heat because the elec-

tron (and hole) relaxes to the conduction (and valence) band edge. The amounts of the losses are around 23% and 33% of the incoming solar energies, respectively (2 in Fig. 2) (1). Eventually, these two mechanisms alone cause the loss of about half of the incident solar energy in solar cell conversion to electricity. Other losses are junction loss, contact loss, and recombination loss which is shown in Fig. 2[1].

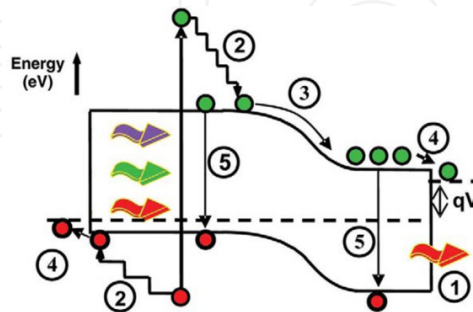


**Figure 2.** Loss processes in a standard solar cell: (1) non absorption of below bandgap photons; (2) lattice thermalization loss; (3) and (4) junction and contact voltage losses; (5) recombination loss (radiative recombination is unavoidable) [2].

Three families of approaches have been proposed for applying multiple energy levels:

1. increasing the number of energy levels;
2. multiple carrier pair generation per high energy photon or single carrier pair generation with multiple low energy photons; and
3. capturing carriers before thermalization.

Of these, tandem cells, an implementation of strategy (a), are the only ones that have, as yet, been realized with efficiencies exceeding the Shockley-Queisser limit [2].

In this chapter, firstly the concept of tandem solar cell or multijunction solar cell will be discussed and then Si nanostructured tandems will be explained precisely. However, amorphous silicon (a-Si) tandems will not be investigated in this chapter due to their lower efficiency in comparison with Si nanostructured tandem solar cells.

#### *Multiple- Junction solar cell*

One of the promising methods to enhance the efficiency of solar cells is to use a stack of solar cells, in which each cell has a band gap that is optimized for the absorption of a certain spectral region [3]. In fact, by stack layers, the number of energy levels is increased. This method was suggested for the first time by Jackson in 1955.

Solar cells consisting of p-n junctions in different semiconductor materials of increasing bandgap are placed on top of each other, such that the highest bandgap intercepts the sunlight first [2].

The importance of multijunction solar cell is that both spectrum splitting and photon selectivity are automatically achieved by the stacking arrangement.

To achieve the highest efficiency from the overall tandem device, the power from each cell in the stack must be optimized. This is done by choosing appropriate bandgaps, thicknesses, junction depths, and doping characteristics, such that the incident solar spectrum is split between the cells most effectively. Moreover two configurations are used for extracting electrical power from the device effectively which are reviewed by Conibeer: either a 'mechanically stacked' cell, in which each cell in the stack is treated as a separate device with two terminals for each; or an 'in-series' cell with each cell in the stack connected in series, such that the overall cell has just two terminals on the front and back of the whole stack. For a fixed solar spectrum and an optimal design, these two configurations give the same efficiency. But for a real, variable spectrum, the mechanically stacked design gives greater flexibility because of the ability to optimize the I-V curve of each cell externally and then connect them in an external circuit.

The reduced flexibility of just optimizing the I-V curve for the whole stack, because the same current must flow through each cell, makes the in series design more sensitive to spectral variations. Furthermore, they become increasingly spectrally sensitive as the number of bandgaps increases. For space-based cells this is not a great problem because of the constant spectrum, but for cells designed for terrestrial use, it is significant because of the variability of the terrestrial solar spectrum. This is particularly the case at the beginning and end of the day when the spectrum is significantly red shifted by the thickness of the atmosphere. Nonetheless, the much greater ease of fabrication of in-series devices makes them the design of choice for most current devices [2].

The efficiency depends on the number of subcells [1]. The efficiency limit for a single pn junction cell is 29%, but this increases to 42.5% and 47.5% for 2-cell and 3-cell tandem solar cells, respectively. However, these values are a little bit more for concentrated light.

For example, the radiative efficiency of bulk silicon (Si) solar cells under the AM1.5G spectrum is limited theoretically to 29% due to the incomplete utilization of high energy photons and transmission of photons with less energy than the Si band gap [3]. But, the theoretical efficiency of tandem solar cells with a bulk Si bottom cell increases to 42.5 % when one additional solar cell with 1.8 eV band gap is used and to 47.5 % with two further solar cells with band gaps of 1.5 and 2 eV placed on top of the bulk Si cell.

#### *Si nanostructure tandems*

Silicon is not suitable for optoelectronic applications because of its indirect bandgap and poor light emission properties. However, silicon bandgap tuning above bulk silicon bandgap (1.12eV) is possible in the nanometer regime (sizes less than 10nm) enabling a revolutionary control over its properties [4]. Therefore, use of nanostructures in tandem solar cells can create bandgap engineering besides improving the efficiency. Improved optical and electrical properties of silicon can be found in different forms of silicon, for example, porous silicon, silicon superlattices and Si-QD embedded in dielectric [4].

In silicon based tandem solar cells, this bandgap engineering can be done using either quantum wells (QWs) or quantum dots (QDs) of Si sandwiched between layers of a dielectric based on Si compounds such as  $\text{SiO}_2$ ,  $\text{Si}_3\text{N}_4$ , SiON or SiC which taking advantages of the

widening of absorption spectrum in the UV range [5]. As a whole, Si nanotechnology is the best choice to improve the metastabilities and to increase the quantum efficiency [6].

By restricting the dimensions of silicon to less than Bohr radius of bulk crystalline silicon (almost 5 nm), quantum confinement causes its effective bandgap to increase. If these dots are close together, carriers can tunnel between them to produce QD superlattices. Such superlattices can then be used as the higher bandgap materials in a tandem cell [1]. In fact, the idea is to add one or more layers of nano-structured materials on the top of a solar cell for which the optical absorption covers different domains of the solar spectrum (Fig. 3 is an example of “all silicon” tandem solar cell).

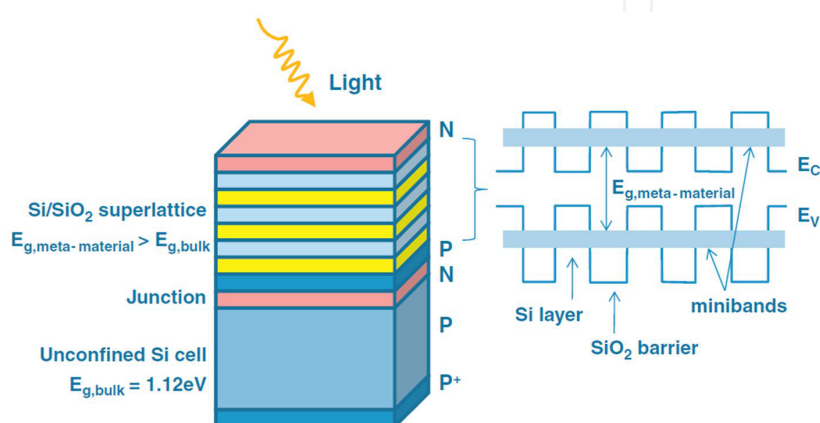


**Figure 3.** Schematics of an “all silicon” tandem solar cell with a top cell based on a nanostructured meta-material stacked on an unconfined Si cell [7].

All tandem solar cells offer the advantages of using silicon which is an abundant material, stable, non-toxic and capable to diversify in order to obtain both a medium bandgap material (~1 eV) and high a bandgap material (~1.7 eV) [7]. It should be mentioned that combining two tandem cell bandgaps (1.12 eV and 1.7 eV) achieve a conversion efficiency factor up to 42%. Another significant advantage of Si is its well developed technology in the world which paves the way for experimental and optimization studies of tandem solar cells. Moreover, strong optical absorption and high photocurrent have been found in nc-Si films and attributed to the enhancement of the optical absorption cross section and good carrier conductivity in the nanometer grains [8].

An approach to prepare silicon quantum dot superlattices by depositing alternating layers of stoichiometric oxide followed by silicon-rich oxide also appears promising in a potentially low cost process, with the control of dot diameter and one spatial coordinate [9]. In detail, these layers are grown by thin-film sputtering or CVD processes followed by a high-temperature anneal to crystallize the Si QWs/QDs. The matrix remains amorphous, thus avoiding some of the problems of lattice mismatch [2]. For sufficiently close spacing of QWs or QDs, a true miniband is formed creating an effectively larger bandgap. For QDs of 2 nm (QWs of 1 nm), an effective bandgap of 1.7 eV results – ideal for a tandem cell element on top of Si [2].

Because of the charge carrier confinement in Si quantum dots it is possible to adjust the band gap by a control of the Si quantum dot size [3].

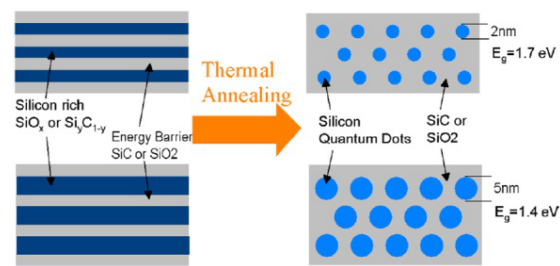


**Figure 4.** Schematic of the procedure to achieve size control of Si NC in Si based dielectric matrices. Layers with silicon excess are deposited alternately between stoichiometric layers. The stoichiometric layers act as a diffusion barrier for the silicon atoms and therefore limit the growth of silicon nanocrystals during the annealing step [3].

Generally, there are two ways for observing and estimating the size [1]:

1. The dot size of the Si QDs can be evidenced by high-resolution transmission electron microscopy (HRTEM). We can clearly see black dots due to contrast difference between Si and  $\text{SiO}_2$  in Fig. 5.
2. Raman spectroscopy can also be used to estimate the dot size. (Fig. 6.)

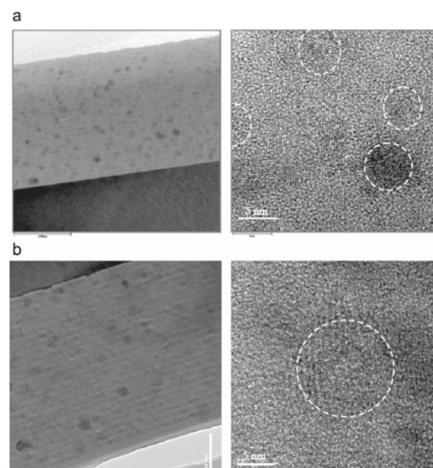


**Figure 5.** Transmission electron microscopy (TEM) images of Si quantum dots in  $\text{SiO}_2$  matrix with low-magnification and high-resolution lattice images for (a) 5 nm Si QDs and (b) 871 nm Si QDs [1].

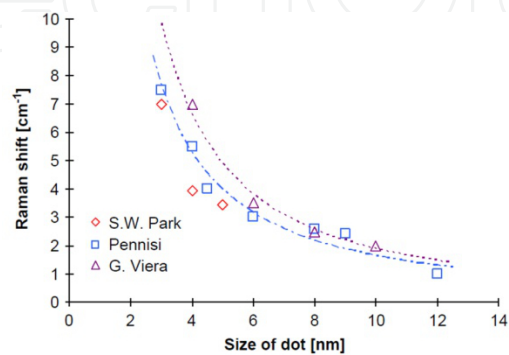


**Figure 6.** Raman peaks shifts to lower energy for Si QDs with 3,4, and 5 nm. Reference data are adapted from Pennisi and co-workers [8] and Viera et al [1].

To realize all-silicon tandem solar cells, Park et al., fabricated phosphorus-doped Si QDs superlattice as an active layer on p-type crystalline Si (c-Si) substrate as shown in Fig. 7. The phosphorous doping in n-type Si QDs superlattice was realized by  $P_2O_5$  co-sputtering during the deposition of silicon-rich oxide (SRO, Si and  $SiO_2$  co-sputtering), which forms Si QDs upon high-temperature post-annealing. The n-type region typically includes 15 or 25 bi-layers formed by alternating deposition of P-doped QDs and  $SiO_2$  [1].

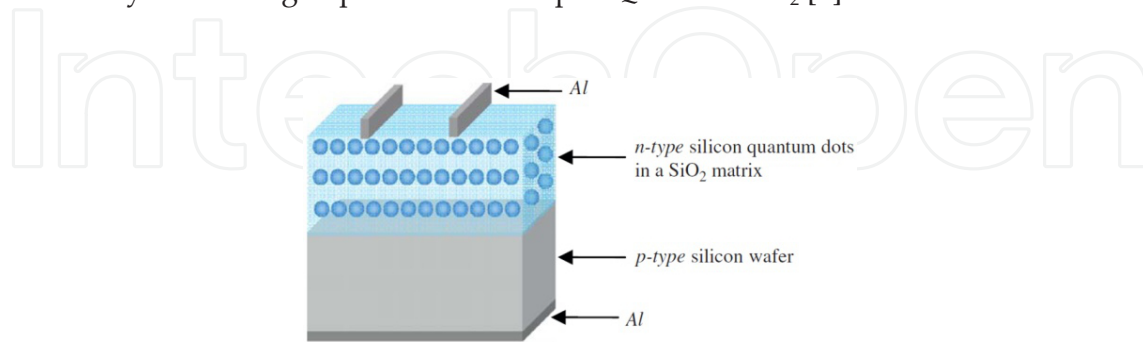


**Figure 7.** Schematic diagram of (n-types) Si QDs and (p-type) c-Si heterojunction solar cell [1].

In the next section the optimization methods for nanostructured silicon based solar cell will be discussed in detail.

### 3. Optimization method in nanostructures

#### 3.1. Silicon quantum dots solar cells

The main challenge for a nanostructure engineered material in a tandem cell is to achieve sufficient carrier mobility and hence a reasonable conductivity. For a nanostructure, this generally requires formation of a true superlattice with overlap of the wave function for adjacent quantum dots; which in turn requires either close spacing between QDs or a low barrier height. Moreover, the quantum confinement, achieved by restricting at least one dimension of silicon less to the Bohr radius of the bulk crystalline silicon (around 5 nm), causes the effective bandgap to increase [10] which also results in increased absorption. The strongest quantum confinement effect is obtained if the silicon is constrained in all three dimensions, as in quantum dots, such that the same increase in effective bandgap can be achieved with a much less stringent size constraint [10]. Different technological approaches allowing formation of Si QDs. Generally, perfect (ideal) QD arrays can have the following characteristics [11]:

1. Absolutely accurate positioning and control for nucleation site of individual QD;
2. Uniformity of size, shape and composition;
3. Large-area ( $\sim cm^2$ ), long-range ordering QDs;
4. The ability to control the QDs size;
5. The ability to achieve both ultra-high dense QD arrays and sparse QD arrays

In this part we will discuss on optimum properties of Si QDs that include size, spacing and dielectric matrix of Si QDs which also have great influences on the band structure [9].

### 3.1.1. Optimum size of Si QDs

A control of the Si nanocrystal size allows the adjustment of essential material parameters such as bandgap and oscillator strengths due to size quantization effects [3]. Experimental results have shown that the size of the QDs can be quite well controlled by selecting an appropriate thickness for the SRO layer and the density of the dots can be varied by the composition of the SRO layer. In detail, the size and crystallization of the Si nanocrystals are dependent on a number of factors, including the annealing method and the barrier thickness [12].

In 2006, Gavin Conibeer et al., at the University of NSW, used the energy confinement of silicon based quantum dot nanostructures to engineer wide band gap materials to be used as upper cell elements in Si based tandem cells. HRTEM data shows Si nanocrystal formation in oxide and nitride matrixes with a controlled nanocrystal size, grown by layered reactive sputtering and layered PECVD [13].

The data shown in Fig. 8 are measured from HRTEM images for samples at several deposition times. There is a sharp decrease in the nanocrystal size distribution on reduction in layer thickness from 4.7 to 3.5 nm. This indicates a transition from a bulk diffusion mechanism of Si atoms during precipitation to a constrained two dimensional diffusion regime, such that the nanocrystal size is defined by the layer thickness [13].

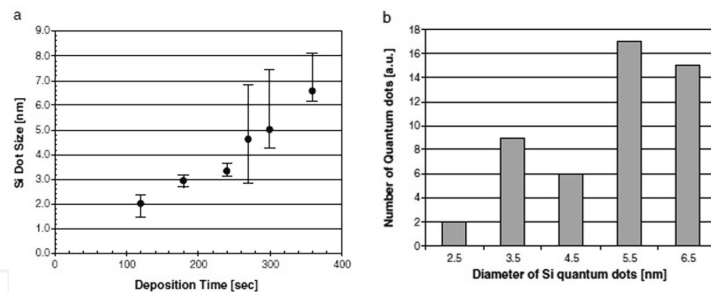


**Figure 8.** a) Dependence of quantum dot size distribution on deposition time as measured by HRTEM (other sputtering parameters optimized). b) QD size distribution for deposition time of 280 s [13].

This is an important self-regulation effect which gives much greater uniformity in nanocrystal optoelectronic properties, at least in the growth direction, as indicated for photoluminescence (PL). PL results indicate quantum confined properties as evidenced by the increase in the photo-luminescent energy in PL experiments [13].

Fig. 9a shows an increase in PL energy as nanocrystal size decreases, thus demonstrating quantum confinement and hence formation of quantum dots. It also shows a dramatic increase in PL intensity on going from a dot diameter of 4.7 to 3.5 nm. This correlates well with the greatly increased uniformity in Si quantum dot size as the deposited layer goes from 4.7 to 3.5 nm, as shown in Fig.8a on change of diffusion mechanism (see above). The

large increase in PL energy is due to the much greater signal at a given energy with good dot size uniformity. (The fact that this intensity drops again is discussed below.) An increase in PL intensity is also to be expected as dot size decreases because of the increase in spatial localization of electrons and holes that will increase the probability of recombination [13].

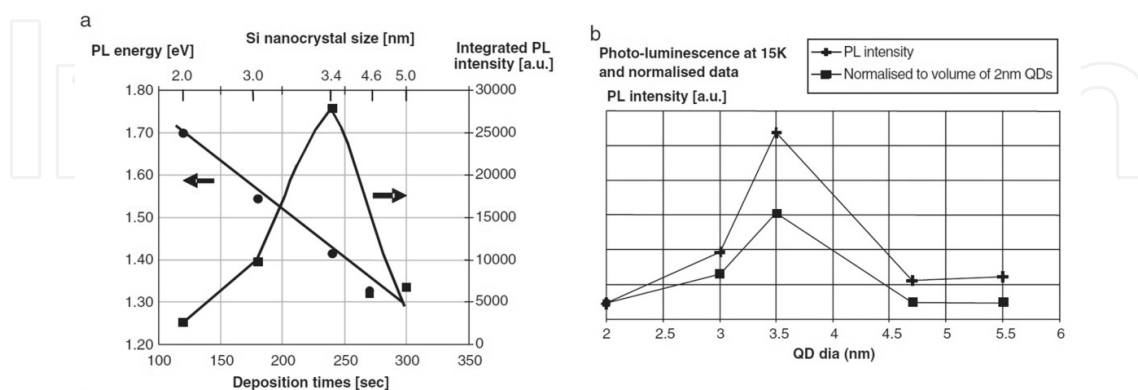


**Figure 9.** a) PL energy and integrated intensity (15 K) as a function of deposition time, showing quantum confined energy in silicon quantum dots. Deposition time is also calibrated for dot diameter by TEM. b) PL intensity data normalized for decreasing volume [13].

Eun-Chel Cho et al. in 2007 in Australia show that there is a large increase in PL intensity as the QD size decreases, which is consistent with the increase in radiative efficiency with the onset of pseudodirectbandgap behavior. The photoluminescence peaks from Si QDs in nitride are more blue-shifted than that of Si QD in oxide. Figure 10 shows the PL peak energies from Si QD dispersed in oxide and nitride. PL peak energies of Si QDs in oxide are less than 2.0 eV, while Si QDs in nitride have peak energies less than 3.0 eV [10].

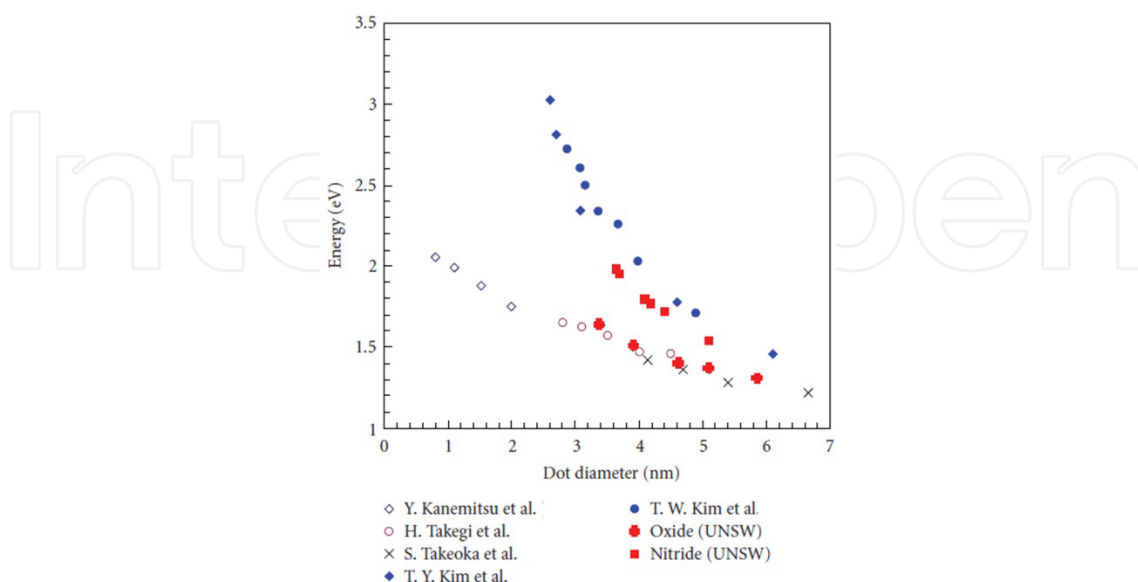


**Figure 10.** Energy gaps of three-dimensionally confined Si nanocrystals in SiO<sub>2</sub> and SiN<sub>x</sub> (300°K) [10].

Puzder et al. in 2002 have explained that the main reason for the PL peak energy reduction in oxide matrix is the distortion of the local  $sp^3$  network by double-bonded oxygen. However, Yang et al. in 2004 claimed that the reason for the stronger blue shift in nitride is better passivation of Si QDs by nitrogen atoms, eliminating the strain at the Si/Si<sub>3</sub>N<sub>4</sub> interface nearly completely [10]. Generally, it can be concluded that the optimum size of Si QDs is 2-3nm.

### 3.1.2. Optimum spacing of Si QDs

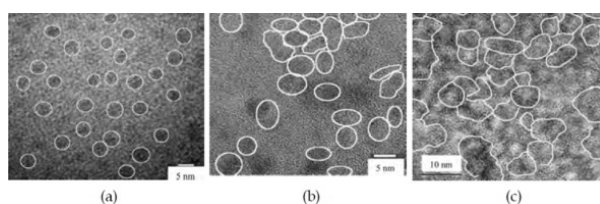
If QDs dots are spaced close enough and there is a significant overlap of the wave function, carriers can tunnel between them to produce a true quantum dot superlattice. Such a superlattice can then be used as the higher bandgap material in a tandem cell [10]. In other words, one common strategy to boost the performance of photovoltaic device structures is incorporating closely packed 3D QD array into device structures. When QDs in different size are formed into an ordered 3D array, there will be strong electron coupling between them so that excitons will have a longer life, facilitating the collection and transport of "hot carriers" to generate electricity at high voltage [11]. In addition, such an array makes it possible to create more than one electron-hole pair from a single absorbed photon, and thus enhance photocurrent, through the process of impact ionization [14]. This process happens when the energy of the photon is far greater than the semiconductor bandgap; while in bulk semiconductors the excess energy is simply dissipates away as heat, in QDs the charge carriers are confined within an infinitesimal volume, thereby increasing their interactions and enhancing the probability for multiple exciton generation [14].

The transport properties of the ensembles of disordered Si QDs in insulating matrix could be explained in terms of the percolation theory, which has already been successfully implemented to explain the transport processes in granular metals by Abeles et al. in 1975. Indeed, this theory describes the effect of the system's connectivity on its geometrical and physical properties [15].

To what concerns the ensemble of Si QDs, there can be distinguished five different structural-electrical regimes, such that in each of them we may expect a different transport mechanism to dominate. These regimes are

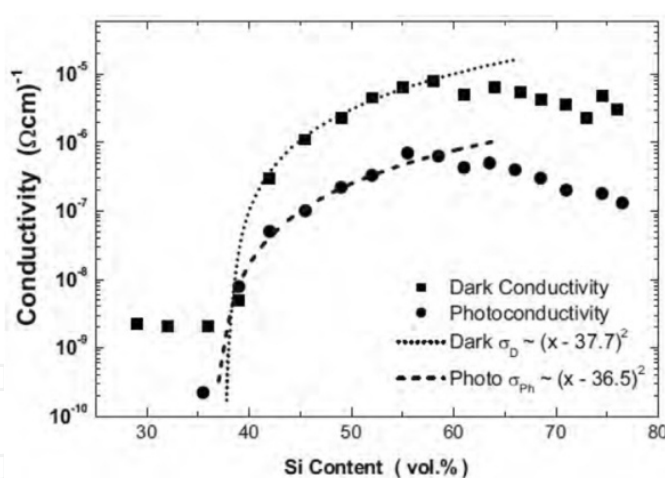
1. Spherical QDs isolated by uniformly dispersed in insulating matrix
2. Some of the QDs starts to "touch" their neighbors named as Transition regime
3. Forming of clusters of "touching" QDs named as Intermediate regime
4. Clusters of regime 3 form a global continuous network named as Percolation transition regime
5. Well forming of percolation cluster of "touching" QDs and disappearance of geometrically non-"touching" QDs.

Fig.11 (a), (b) and (c) present typical examples of ensembles of Si QDs corresponding to regimes 1, 3 and 5, respectively. Usually there are narrow (no more than 0.5 nm wide) boundaries formed between the nanoparticles, which involves at least a different crystallographic orientation of the touching crystallites. In a literature the charge transfer process between such "touching" QDs was termed as "migration".



**Figure 11.** HRTEM images of the ensembles of Si QDs corresponding to different structuralelectrical regimes: (a) uniformly dispersed isolated spherical QDs (regime 1), (b) clusters of “touching” QDs (regime 3) and (c) percolation clusters of “touching” QDs (regime 5)[15].

The effect of the connectivity on the transport properties (dark and photoconductivity) of the ensembles of Si QDS is illustrated in Fig. 12. As one can see, the global picture of transport in Si QDs ensembles is reminiscent of that of granular metals, but the details are quite different. As long as Si QDs or clusters of Si QDs are small enough, they “keep” the carrier that resides in them and become charged when an excess charge carrier reaches them. Hence, the transport through the system can take place only if a corresponding charging (or Coulomb) energy is provided [15]. Balberg et al. in 2004 reported this topic for the samples with low number of Si QDs in the ensemble, which are characterized by the QDs of regime 1, the local conductivity is determined by the tunneling of charge carriers under Coulomb blockage between adjacent nanocrystallites similar to the case encountered in granular metals in the dielectric regime.



**Figure 12.** Dependence of the dark conductivity and the photoconductivity on the Si content [15].

With increasing of Si content (Figure 11b), the interparticle distance decreases and the tunneling-connected quantum dot clusters grow in size. The “delocalization” of the carrier from its confinement in the individual quantum dot to larger regions of the ensemble will take place, i.e., the charge carrier will belong to a cluster of QDs rather than to an individual QD. Correspondingly, this will also yield a decrease in the local charging energy in comparison with that of the isolated QD and the distance to which the charge carrier could wander will increase and as a consequence the conductivity of the ensemble will increase as well. The

charge carrier transport in the case of regime 3 is thus determined by the intracluster migration and by the intercluster tunneling.

Finally we can conclude from Fig. 12 that the maximal possible conductivity is assured regime 5 and the highly percolating system of Si QDs will ensure the most favorable conditions for the electronic transport between the nanocrystals and the bandgap value in such structures can be adjusted in the large range covering the major part of the solar spectrum.

Also transport properties are expected to depend on the matrix in which the silicon quantum dots are embedded. As shown in Figure 13, different matrices produce different transport barriers between the Si dot and the matrix, with tunneling probability heavily dependent on the height of this barrier.  $\text{Si}_3\text{N}_4$  and SiC give lower barriers than  $\text{SiO}_2$  allowing larger dot spacing for a given tunneling current [13].

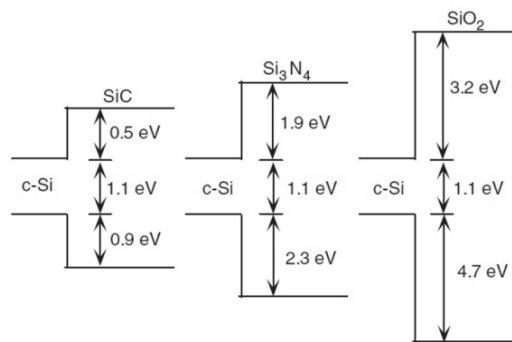


**Figure 13.** Bulk band alignments between crystalline silicon and its carbide, nitride and oxide [13].

The results suggest that dots in a  $\text{SiO}_2$  matrix would have to be separated by no more than 1-2 nm of matrix, while they could be separated by more than 4 nm of SiC [10]. It is also found that the Bloch mobilities do not depend strongly on variations in the dot spacing but do depend strongly on dot size within the QD material [16].

Hence, transport between dots can be significantly increased by using alternative matrices with a lower barrier height,  $\Delta E$ . The spacing of dots would have to be closest in the oxide, nitride and carbide, in that order. Similar deposition and quantum dot precipitation approaches should work for all [16].

### 3.1.3. Optimum dielectric matrix of Si QDs

In recent years it emerged that the Si QD interface with its surrounding dielectric matrix plays a decisive role in determining the optical absorption gap and the optical activity of the Si QD on both experimental and theoretical grounds [17].

Generally, as mentioned above, three types of dielectric matrices  $\text{SiO}_2$ ,  $\text{Si}_3\text{N}_4$ , or SiC are used to form all tandem silicon solar cell.

It should be considered that lower barrier heights will give a greater tunneling probability between adjacent Si QDs and hence greater conductance [18]. Therefore,  $\text{Si}_3\text{N}_4$  and SiC have

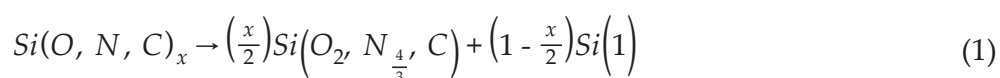
greater conductance than SiO<sub>2</sub>. In detail, SiC has the lowest barrier height among these dielectrics. However, the low barrier height also limits the minimum size of QDs to about 3nm or else the quantum-confined levels are likely to rise above the level of the barrier, which should be around 2.3 eV for amorphous SiC. In addition, although SiO<sub>2</sub> matrix has higher barrier height (3.2eV) comparatively, many attempts were made to fabricate Si-QD in Si-rich SiO<sub>2</sub> thick layers or superlattices since SiO<sub>2</sub> is a frequently used dielectric and compatible in microelectronics processes [4].

Si ion implantation into an oxide layer can be used to produce Si QDs at an irregular position with a relatively large size distribution. Si QDs can fabricate by solution synthesis, mechanical milling, and particle selection from porous silicon, but it is difficult to control the size uniformity of distributed QDs or an additional process to select the particle with the same size [15].

The material requirements for the dielectric layers are ease of thin-film growth and use of abundant nontoxic materials, hence it is most likely to be an oxide, nitride, or carbide of silicon. It is also necessary that carriers from the quantum dot layers have a high probability of tunneling through the dielectric layers [10]. It is worth noting that these devices must be thin to limit recombination due to their short diffusion lengths, which in turn means they must have high absorption coefficients [18]. For layers of thickness less than about 4 nm, the precipitation enters a regime of 2D diffusion in which the dot size is accurately controlled by the layer thickness [13]. This is achieved by creating each dielectric layer with a thickness in the range of 1.5 to 2.5 nm for the case of oxide [10].

Si QD fabrication by various vacuum deposition techniques is preferable because of the greater potential of integration into conventional devices [10]. These include sputtering and plasma enhanced chemical vapor deposition (PECVD). The most successful and hence most commonly used technique is sputtering, because of its large amount of control over deposition material, deposition rate and abruptness of layers. This uses a new multi-target remote plasma sputtering machine with two independent RF power supplies as well as an additional DC power supply [16].

Si precipitation from a Si-rich layer, high temperature annealing of excess Si in an inert atmosphere is necessary to form Si nanocrystals with a few nm diameters, for example, Si QD precipitation in oxide, nitride, and carbide (Figure 14.a) and Equation (1) describes this Si precipitation mechanism [10]:



It should be mentioned that in particular the amount of excess silicon in the Si-rich layer is an important parameter to study the nucleation of the QDs. If the Si concentration in the Si-rich layer film before annealing exceeds a certain limit, dots can merge together during the coalescence phase of the growth process, affecting the quantum confinement properties of the structures [25].

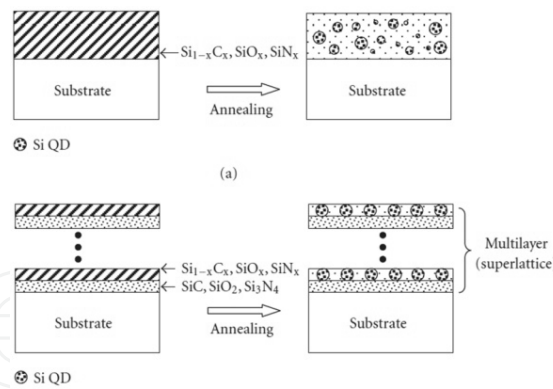


**Figure 14.** Si QDs from phase separation of a) a single silicon-rich precursor layer and b) a multilayer structure [10].

More accurate size control and a narrow size distribution are achieved by growth of a Si QD multilayer structure, which is fabricated by alternating layers of stoichiometric insulating materials and silicon-rich layers shown in Figure 14 b. Depending on the annealing conditions, silicon precipitates from the silicon-rich layers as approximately spherical QDs of a diameter close to the original layer thickness. Hence controls of the diameter and of one spatial coordinate of the dots are possible.

As mentioned above, SiO<sub>2</sub> is a frequently used dielectric and compatible in microelectronics processes. Therefore, Si-QD is generally fabricated in Si-rich SiO<sub>2</sub> thick layers or superlattices. Another dielectric option is SiN<sub>x</sub> dielectrics. Due to low barrier height, highest Si-QD growth density in Si<sub>3</sub>N<sub>4</sub> and less silicon requirement in Si<sub>3</sub>N<sub>4</sub> during deposition, this dielectric is replaced instead of SiO<sub>2</sub>. Moreover, the formation of Si-QD in SiN<sub>x</sub> is preferable, because the formation of 3–7 nm Si-QD in Si-rich SiC film requires higher thermal budget (1100 °C) than Si-QD formation in a-Si/SiN<sub>x</sub> layer structure that requires lower annealing temperature (800–850°C) [4].

Efficient photoluminescence (PL) has also been observed from Si-rich SiN<sub>x</sub> films, a single Si-QD layer sandwiched between two a-SiN<sub>x</sub> layers and structured layers of Si-QD in a-SiN<sub>x</sub>. In addition, for the same Si-QD size and PL excitation wavelength, Si-QDs in SiN<sub>x</sub> film show PL peak in shorter wavelengths (450–620 nm) than Si-QDs in SiO<sub>2</sub> film (650–950 nm) [4]. TEM images in Figure 8 show Si QDs interspersed in the oxide matrix [10].

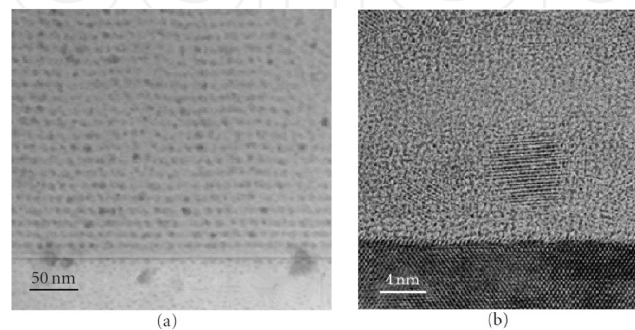


**Figure 15.** Transmission electron microscopy (TEM) images of Si QDs in SiO<sub>2</sub> matrix with (a) low magnification and (b) HRTEM lattice image of Si quantum dots [10].

The bandgap of  $\text{Si}_3\text{N}_4$  is significantly lower than that of  $\text{SiO}_2$ . Hence Si QDs in the nitride offer a lower barrier height and much increased carrier tunneling probability between quantum dots. (SiC offers a lower barrier still.) For this reason, Si QDs have explored transferring the technology in  $\text{SiO}_2$  to the growth of Si nanocrystals in silicon nitride by both sputtering and PECVD [10].

Layered Si QDs have also extended the in nitride technology to gas phase in situ deposition. Figure 16 shows in situ Si QD dispersed in a nitride matrix. A stoichiometric  $\text{Si}_3\text{N}_4$  layer and an in situ Si QD layer are alternately deposited on a Si substrate. This technique allows QDs to form during deposition without a postdeposition annealing. This technique is a low temperature process and may be potentially beneficial to doping of Si QDs owing to high equilibrium temperature of the plasma and free of high temperature postannealing described in Figure 14 [16].

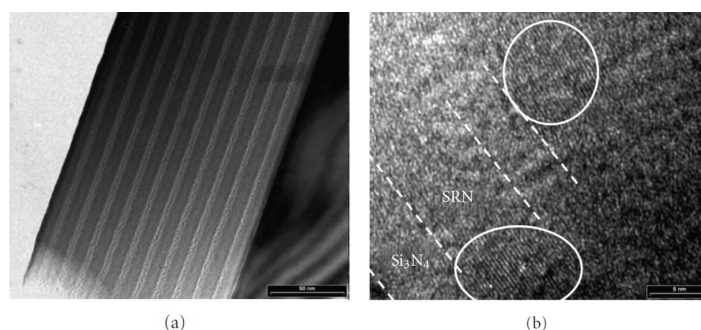


**Figure 16.** Si QDs dispersed in a  $\text{Si}_3\text{N}_4$  matrix fabricated by gas phase in situ deposition: a) low-magnification TEM and b) high-resolution TEM [10].

Another dielectric for growing Si-QD is SiC. Although the electron tunneling conductivity is higher in SiC compared to  $\text{Si}_3\text{N}_4$  and  $\text{SiO}_2$  due to the lower barrier height (0.5eV) of SiC; the formation of Si-QD in  $\text{SiN}_x$  is preferable, because the formation of 3–7 nm Si-QD in Si-rich SiC film requires higher thermal budget (1100°C) than Si-QD formation in a-Si/ $\text{SiN}_x$  layer structure that requires lower annealing temperature (800–850°C) [4].

After annealing above 1000°C, indicating formation of amorphous graphitic carbon is indicated. Hence the best data so far for Si nanocrystals in a SiC matrix are obtained for a  $\text{Si}_{0.75}\text{C}_{0.25}$  precursor composition [10].  $\text{Si}_{1-x}\text{C}_x/\text{SiC}$  multilayers have also been deposited by sputtering to give better control over the Si QD as with oxide and nitride matrices [18].

Raman, TEM and XRD spectra for a silicon-rich  $\text{Si}_{0.75}\text{C}_{0.25}$  precursor layer grown on a quartz substrate with subsequent annealing are shown in Figure 17. There is clear evidence for the formation of nano-crystalline Si at an annealing temperature greater than 1000°C. This is shown in the Raman peak at  $\sim 508 \text{ cm}^{-1}$  (red shifted from  $520 \text{ cm}^{-1}$  due to a nanocrystalline folded Brillouin zone dispersion in k-space); TEM lattice fringe spacing consistent with  $\{111\}$  Si planes; and XRD peaks at  $2\theta = 28.40$  with peak broadening indicating nanocrystal of 3–7nm (estimated using the Scherrer equation). It should be noted that here the nanocrystal size determined by TEM is slightly smaller than that determined by XRD[10].

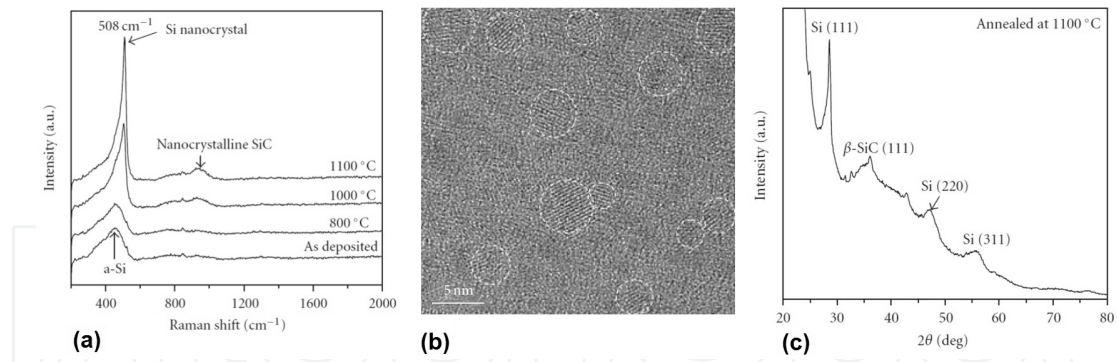


**Figure 17.** Silicon-rich SiC precursor layer: (a) Raman spectra for various annealing temperatures; Cross-sectional HRTEM image; and (c) X-ray diffraction [10].

Other Si and C concentrations were tried. As the concentration of C in  $\text{SiC}_x$  is increased to the nearly stoichiometric  $\text{Si}_{0.495}\text{C}_{0.505}$ , Raman evidence for the stretching vibration modes of Si-C and C-C bonds can be easily identified. With increasing annealing temperature, which shows increasing intensities of both TO and LO bands, the formation of crystalline SiC during annealing is indicated. In addition, there is a dramatic decrease in the intensity of Si-Si vibration modes indicating the formation of far fewer Si nanocrystals. There is also evidence for free carbon at  $\sim 1400\text{ cm}^{-1}$  in as deposited film, splitting into two bands at  $\sim 1360$  (D band) and  $1590\text{ cm}^{-1}$  (G band) [16].

As before, a multilayer approach was used to fabricate Si QDs in carbide of uniform size. A multilayer with stoichiometric SiC and silicon-rich  $\text{Si}_{1-x}\text{C}_x$  precursor layer was fabricated, as shown in Figure 17.a, and annealed at a high temperature to selectively precipitate Si nanocrystals in a carbide matrix. However, the lattice fringes in HRTEM image correspond to  $\beta\text{-SiC}$  {111} crystalline planes (Figure 17.b). One possible reason for SiC QDs, instead of Si QDs, is that the C/Si ratio in layered structure has an increase, compared to the original design.

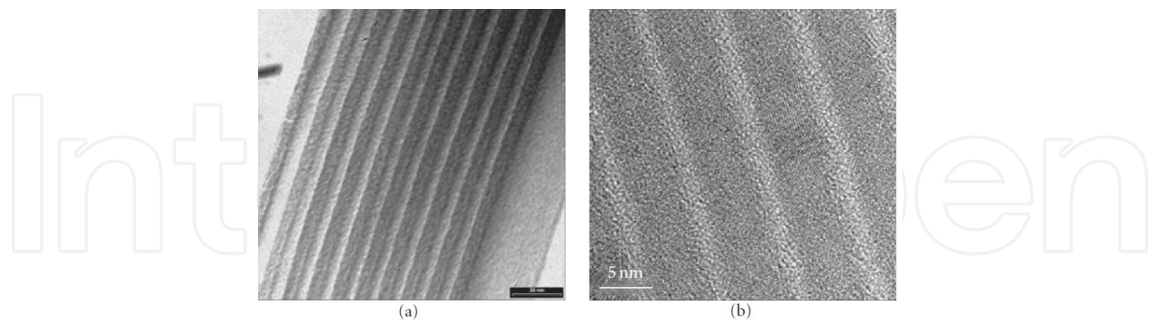


**Figure 18.** TEM images of SiC/Silicon-rich SiC multilayer a) deposited and b) annealed at  $1100^\circ\text{C}$  for 20 minutes [10].

The decay length  $L_d$  is determined by the barrier height of the material in which the dot is embedded, which in the present case is either a silicon carbide, nitride, or oxide matrix [10]. In the simplest case, the decay length ( $L_d$ ) is given by:

$$L_d = \frac{1}{\sqrt{2m^*(V_0 - E_n)}} \quad (2)$$

The latter expression holds when  $\Delta E$ , the difference between the conduction band edge of the matrix and the confined energy level, is in  $\text{eV}\cdot\text{m}^*$  and  $m_0$  are the effective mass and electron mass in the matrix material, respectively.  $V_0$  is the corresponding band offset and  $E_n$  is the confined energy level in a quantum dot. Without considering the confined energy of QDs, energy difference  $\Delta E$  are 3.2 eV, 1.9 eV, and 0.5 eV for the conduction edge of bulk Si and  $\text{SiO}_2$ ,  $\text{Si}_3\text{N}_4$ , and SiC, respectively. Electrons effective masses of  $\text{SiO}_2$ ,  $\text{Si}_3\text{N}_4$ , and 3C-SiC are 0.86, 0.05–0.13 [19], and  $0.24 \pm 0.1$ , respectively. Following this line of argument, the results suggest that dots in an  $\text{SiO}_2$  matrix would have to be separated by no more than 1-2 nm of matrix for a reasonable overlap of the wave function and hence of conductivity, while they could be separated by more than 4nm of SiC [10].

### 3.2. Silicon nanowire solar cells

The semiconductor nanostructures are hence proposed to combine with the organic materials to provide not only a large interface area between organic and inorganic components for exciton dissociation but also fast electron transport in semiconductors. Therefore, many research groups combined organic materials with semiconductor nanostructures to overcome the drawbacks of the organic solar cells. Many inorganic nanowires had been experimented for this purpose, including CdTe, CdS, CdSe, ZnO, and  $\text{TiO}_2$  nanowires [20]. To overcome this Silicon nanowires (SiNWs) have attracted much attention for photovoltaic applications because of their unique optical and electrical properties [21] and have the potential to impact many different technologies either through improved material properties or by offering a new geometry not possible with bulk or thin film devices [22]. It is known that SiNW arrays demonstrate excellent antireflection (AR) properties due to their broadband optical absorption by multiple scattering incidents, and therefore can be used as solar cell absorbers for trapping light [21]. In practical applications, a bunch of SiNWs are more useful than a single SiNW. The usage of SiNW arrays can be categorized into two types. The first one is for anti-reflection purposes. SiNW arrays are used to replace the conventional anti-reflection coating layer. The second one is SiNW-array core-sheath p-n junction solar cells. In particular, the second type combines the advantages of the first type, that is, a large junction area, a high anti-reflection ability, and a high light-trapping effect [23].

SiNWs can be prepared by fabricated by various techniques, including chemical vapor deposition (CVD), physical vapor deposition (PVD), reactive ion etching (RIE) combined with lithography techniques [22], dry etching, laser ablation, and vapor-liquid-solid (VLS) [20]. Among these, the metal-assisted chemical etching (MACE) technique is more facile and more economical to fabricate SiNW arrays since it avoids high temperature or high vacuum [22].

Fabrication of nanowire based solar cells with nanowire arrays formed on the entire wafer by the wet etch process has obtained a very reasonably good energy conversion efficiency. However, with the formation of SiNW arrays by VLS process on the entire silicon wafer, the solar cell performance is very poor and has an energy conversion efficiency of only 0.1% [24] due to improper doping condition used.

The SiNW arrays have been demonstrated as an efficient antireflection film for silicon solar cell by proper growth of density and length of wires [24]. Fabrications of these wires on si substrate, nanowire length has linear behave by etching time. Zeng et al. confirmed this with their experiments. The SEM observation clearly revealed that the lengths of the produced SiNWs increased with the etching time, ranging from 340nm to 1700nm, which indicates that the length of the SiNWs can effectively be tailored by prolonging the etching time. Fig. 19(f) shows the SiNW length as a function of the etching time. An excellent linear behavior can be obtained.

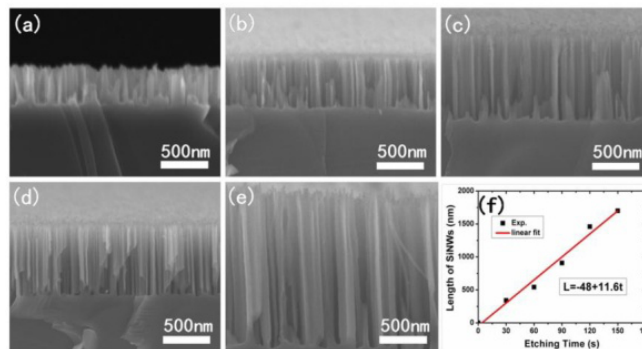


**Figure 19.** a-e) demonstrates the cross-sectional SEM micrographs of SiNW arrays with different length fabricated at 0.2 M H<sub>2</sub>O<sub>2</sub> and room temperature for 30s, 60s, 90s, 120s, and 150s, respectively. (f) shows the SiNW length as a function of the etching time [21].

Also the thickness of SiNWs has impressive on solar cell spectrum absorption and the optimum length of nanowires for 350 to 620 nm. Huang et al. in 2009 was confirmed on that by combination of the SiNWs and P3HT:PCBM blend is an attractive route to obtain high  $J_{sc}$  and efficiencies by improving the optical absorption, dissociation of excitons, and the electron transport. The P3HT:PCBM film exhibits little absorption beyond 650nm. The SiNWs/P3HT:PCBM film has improved light harvesting from 650 to 1100 nm because the cut off wavelength of Si is about 1100nm (Figure 20(Left)) [20].

Zeng et al. also shows that the as-grown SiNW arrays exhibit not only a large suppression of the reflectance over the entire light wavelength range, but also a very different reflection behavior from polished Si. The reflectance decreases with the wavelength increasing. As shown in figure 20(b), the reflectance is smaller than 18%, 9%, 5%, 2% and 1% at the nanowires length of 340nm, 542nm, 908nm, 1460nm and 1700nm, respectively. This can be attributed to the three important properties of SiNW arrays [21]:

1. The extremely high surface area of the SiNW arrays.
2. The suppression of the reflectance over a wide spectral bandwidth due to the subwavelength-structured (SWS) surface of the SiNW arrays.
3. A gradual change in the refractive index with depth due to a porosity gradient throughout the SiNW arrays which closely resembles a multi-antireflection layer coating.

It should also be mentioned that the interference peaks in the reflectance spectra of the SiNW arrays are related to the periodic nanostructure nature to some extent.

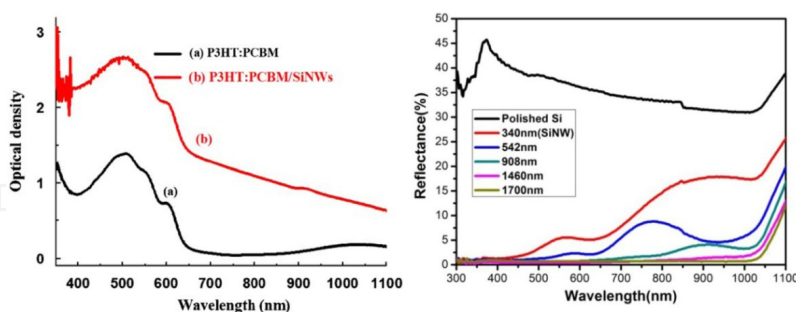


**Figure 20.** Left) UV–visible absorption of P3HT:PCBM blend on the ITO glass (a) with SiNWs and (b) without SiNWs. Right) Reflectance of SiNWs and polished wafer as a function of light wavelength, nanowires length of 340nm, 542nm, 908nm, 1460nm and 1700nm [20,21].

Also the SiNW arrays grown on the silicon substrate with  $\text{SiH}_4:\text{N}_2$  gases exhibit good optical characteristic of antireflection with same result as mentioned [24]. On the other hand, it is also expected that the long SiNWs will have more light-trapping effect than the short SiNWs. The reflectance measurement does confirm this speculation because the reflectance decreases with the wire's length, as shown in Figure 20. However, this is not consistent with the devices' performance because the device with the shortest wire length has much better performance than the one with the longest length [23].

In addition, the reflectance decreases as the wire length increases. The reason can be easily explained by the enhanced light-trapping effect caused by the increasing wire length. However, this cannot explain the better performance of the device with a shorter wire length than that with a longer SiNWs [23].

Comparison of the photovoltaic performance for SiNW solar cells with SiNWs grown at different conditions. Figure 21 shows the device parameters, including the cell areas, and current density-to-voltage (J-V) curves under 1 sun AM 1.5 G illumination. The  $0.37 \mu\text{m}$ -SiNW/PEDOT:PSS solar cell has the highest PCE of 8.40%, highest  $J_{sc}$  of  $24.24 \text{ mA}/\text{cm}^2$ , and highest  $V_{oc}$  of 0.532 V. When the SiNWs' length extends to  $5.59 \mu\text{m}$ , PCE reduces from 8.40% to 3.76%,  $J_{sc}$  decays from  $24.24 \text{ mA}/\text{cm}^2$  to  $13.06 \text{ mA}/\text{cm}^2$ ,  $V_{oc}$  decreases from 0.532 V to 0.435 V, and  $R_s$  increases from  $2.95 \Omega \text{ cm}^2$  to  $4.25 \Omega \text{ cm}^2$ . Only fill factor (FF) stays in the range between 63% and 67% [23].

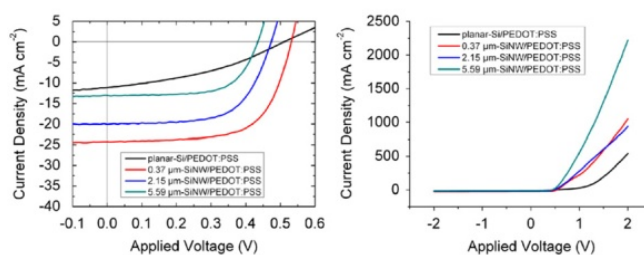


**Figure 21.** Current density-to-voltage curves of each SiNW devices and planar Si devices under the illuminance condition of 1 sun AM 1.5 G. (Left) Curves around fourth quarter. (Right) Curves in the range of -2 V to 2 V [23].

However, the I–V characteristic measurements of this SiNW-based photovoltaic cell still indicate a much lower short circuit current, leading to much lower energy conversion efficiency in comparison with planar or textured Si solar cell. The much lower short circuit current is attributed to the lower density of the nanowire grown by the current VLS process, which could not provide efficient light trapping and causes large series resistance in the SiNW network [24].

At least the current SiNWs based solar cells have a much better performance than the ones reported in the literature, there is still much room to improve the performance by growing denser arrays of nanowires, which provide enough light trapping and reduce series resistance, and by growing nanowires with less amount of metal catalysts or other catalysts that do not cause recombination centers [24].

## 4. Structural and superficial optimization

There are a number of structural optimization methods that can improve the efficiency besides process optimization which is discussed in previous section. Such as surface texturing, anti-reflection coating, defect passivating by forming gas, use of concentrator system, etc. In this section the last two methods will be discussed more.

### 4.1. Concentrator Photovoltaics

To moderate the price of multijunction solar cells and also to increase the efficiency, optical concentrator systems are proposed. The key elements of a photovoltaic concentrator are low-cost concentrating optics (a system of lenses or reflectors) to focus sunlight on a small area of solar cells, mounting, single or dual-axis tracking to improve performance of the system, and high-efficiency solar cells[14].

Theoretical maximum efficiencies of multi-junction solar cells without concentration and for concentration ratio of 500x have large difference. For example, the efficiency is 30.8% and 49.3% at one sun for one and three junction solar cell respectively, but it increases to 40.8% and 63.8% under concentration [14].

The first concentrator photovoltaic system was proposed in the mid 1970's by Sandia Labs. Despite the advantages of concentrating technologies, their application has been limited by the costs of focusing, tracking and cooling equipment. Optimization of a concentrator system is a complex problem: as all its components like solar cells, optics and tracking systems have to be specifically optimized, and all the interactions have to be regarded [14]. Natalya V. Yastrebova has reported several effective concentrator designs: Amonix is installing 250x concentrators using Fresnel lenses; Solar Systems, Spectrolab and Concentrating Technologies are installing reflective dishes; SunPower is designing a high-concentration, thin (flat-plate-like) concentrator; the Ioffe and Fraunhofer Institutes are developing a 130x glass-Fresnel concentrator (Figure 22).

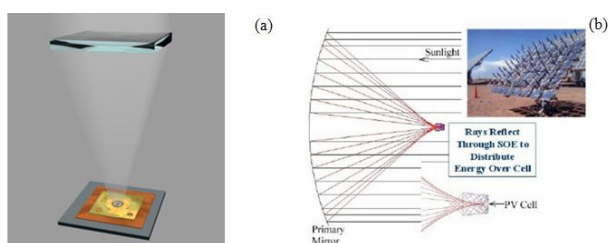


**Figure 22.** a) Concentrix concentrator using Fresnel lenses b) Spectrolab's reflective-optics concentrator module [14].

However, it should be taken into account that concentrators require direct sunlight and hence do not work with an overcast sky. Therefore, the concentrators are suitable for areas where cloud cover is low. The most appropriate time for operation is the middle of the day when the sunlight is strongest because at this time, the spectrum is least variable and hence spectral sensitivity is less significant [13].

#### 4.2. Passivating the interfacial defects

One of the methods to enhance photoluminescence properties of nanostructured silicon based solar cells is passivating the non-radiative defects at the Si-barrier ( $\text{SiO}_2$ ,  $\text{Si}_3\text{N}_4$ ,...) interface by a forming gas (FG) post hydrogenation process performed on structures previously annealed in  $\text{N}_2$  for different durations as proposed by Aliberti et al. A significant enhancement of the PL intensity has been observed for the samples with QD nominal size larger than 4nm, whereas a moderate enhancement is shown for the samples with QD size smaller than 4nm (Figure 23.a)[25].

Figure 23 b shows the PL spectra for two samples with a single layer of Si QDs in  $\text{SiO}_2$  before and after FG hydrogenation. One sample has nominally 6 nm Si QDs and the other has 3.6 nm Si QDs. In addition to the intensity increase, which is more pronounced for the sample with larger QDs, no significant variation of the PL peak energy, or appreciable difference of the shape of the PL signal, can be observed in any of the samples [25].

The fact that the PL peak energy remains unmodified after the FG hydrogenation is an indication that, for sputtered single layer Si QDs in  $\text{SiO}_2$ , the PL cannot be attributed to defects. Therefore, the PL of these structures relies entirely on the quantum confinement effect of Si QDs[25].

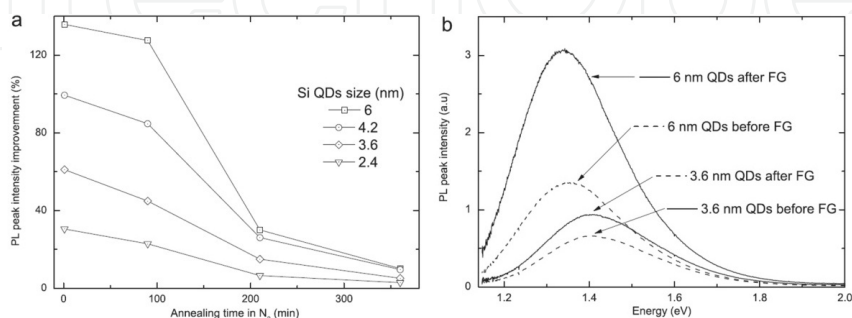


**Figure 23.** a) Relative improvement of the PL peak intensity for single layer Si QDs in  $\text{SiO}_2$  samples after FG post-hydrogenation versus annealing time in  $\text{N}_2$  (before FG) b) PL signal of two samples with different QDs nominal size (6 and 3.6 nm) before and after FG post-hydrogenation (samples have been annealed in  $\text{N}_2$  at 1100°C for 5 min) [25].

## 5. Conclusions and outlook

Third generation nanostructured silicon based solar cells offer significantly lower cost per Watt by applying multiple energy levels with abundant and nontoxic material that also benefits from thin film processes.

Therefore, optimization of these high efficient solar cells is a demand which should be satisfied by detailed researches. Then, in this chapter, various optimization methods have been taken into account.

The first is optimization in silicon quantum dot solar cells. We conclude that the control over QD size is possible for layer thicknesses less than about 7nm, within which Si migration to nucleating sites is dominated by a 2D rather than a 3D diffusion regime. For this layer thickness, the optimum size for Si QDs is 2-3 nm.

Moreover, to ensure favorable electronic transport, the optimum spacing should be satisfied. We conclude that in lower spacing, the possibility of percolation is enhanced; then the prominent regime will be charge transfer which is called migration instead of electron tunneling. It should be paid attention that different matrices produce different transport barriers between the Si QDs and the matrices, because tunneling strongly depends on the height of barrier. So,  $\text{Si}_3\text{N}_4$  and SiC allow larger spacing for a given tunneling current in comparison with  $\text{SiO}_2$  because they give lower barriers.

Although the electron tunneling conductivity is higher in SiC compared to  $\text{Si}_3\text{N}_4$  and  $\text{SiO}_2$  due to the lower barrier height (0.5eV) of SiC; the formation of Si-QD in  $\text{SiN}_x$  is preferable, because the formation of 3-7 nm Si-QD in Si-rich SiC film requires higher thermal budget (1100°C) than Si-QD formation in a-Si/ $\text{SiN}_x$  layer structure that requires lower annealing temperature (800-850°C).

Also, we conclude that Si QD fabrication by various vacuum deposition techniques is preferable because of the greater potential of integration into conventional devices.

The second is optimization in silicon nanowire solar cell which explains that in some aspects, Si NW is preferable in comparison with Si QD. The most important feature of SiNW is its crystallinity invariance under introduction of impurity atoms during the growth. In other words, SiNW is well-defined doped nanocrystal during synthesis. Moreover, it demonstrates ultra-high surface area ratio, low reflection, absorption of wideband light and tunable bandgap.

In addition, the absorption in Si NW is more than solid Si film. And in order to optimize SiNW, wire diameter, surface conditions, crystal quality and crystallographic orientation along the wire axis should be investigated. In practice, radial p-n junction NW cells tend to favor high doping levels to produce high cell efficiencies (up to 11%). Therefore, solar cells based on arrays of Si wires are a promising approach to reducing the cost of solar cell production.

However, SiNW has some disadvantages. For example, the probe light used in the optical measurement cannot be focused solely onto the nanowire.

In addition to above mentioned process optimization, structural optimization is discussed briefly. As a result, concentrator systems and forming gas can ensure the high efficiency nanostructured Silicon based solar cells.

This chapter brings an overview about various optimization methods which can be done over third generation nanostructured silicon based solar cells, however, there is a long way to achieve optimum values experimentally. So, more experimental researches in this area are required.

## Acknowledgements

The authors want to thank INI (Iran Nanotechnology Initiative) Council and Student Scientific Association of University of Tabriz for their support. And, also they are very grateful to Dr. Rostami, Dr. Rasouli and Dr. Baghban who help them to do research in this field of photovoltaics.

## Author details

Foozieh Sohrabi<sup>1\*</sup>, Arash Nikniazi<sup>2</sup> and Hossein Movla<sup>2</sup>

\*Address all correspondence to: F.sohrabi90@ms.tabrizu.ac.ir

1 School of engineering emerging technologies, University of Tabriz, Tabriz, Iran

2 Faculty of Physics, University of Tabriz, Tabriz, Iran

## References

- [1] Park, S, Cho, E, Song, D, Conibeer, G, & Green, M. A. (2009 ). Cells n -Type silicon quantum dots and p-type crystalline silicon heteroface solar cells. *Solar Energy Materials & Solar*, 93684-690.
- [2] Conibeer, G. (2007). Third-generation photovoltaics. *Material Today*, 10(11), 44-50.
- [3] Löper, P, Hiller, D, Janz, S, Hermle, M, Glunz, S.W., & Zacharias, M. (2011). 23rd Workshop on Quantum Solar Energy Conversion. 20-26 March 2011, Bad Hofgastein, Austria.
- [4] Panchal, A.K., & Solanki, C.S. (2011). Fabrication of silicon quantum dots in SiN<sub>x</sub> multilayer using hot-wire CVD. *Journal of Crystal Growth*, 3112659-2663.
- [5] Gourbilleau, F., Dufour, C., Rezgui, B., & Brémond, G. (2009). *Materials Science and Engineering B*. 15970-73.

- [6] Shen, W. Z. (2011). Silicon Quantum Dots: Photoluminescence Controlling and Solar Cell Application. *Seventh International Conference on Thin Film Physics and Applications*.
- [7] Munteanu, D, & Autran, J. L. (2011). Modeling of energy bands in ultra-thin layer quantum nanostructures for solar cell applications. *Journal of Non-Crystalline Solids*, 357, 1884-1887.
- [8] Xu, C., Li, Z. P., Pan, W., & Shen, W. Z. (2011). Tuning photoresponse through size distribution control of silicon quantum dots. *Applied Surface Science*, 2578409-8412.
- [9] Jiang, C, & Green, M. A. (2006). Silicon quantum dot superlattices: modeling of energy bands, densities of states, and mobilities for silicon tandem solar cell application. *Journal of applied physics*, 99114902.
- [10] Cho, E., Green, M. A., Conibeer, G., Song, D., Cho, Y., Scardera, G., Huang, S., Park, S., Hao, X. J., Huang, Y., & Dao, L. V. (2007). Silicon Quantum Dots in a Dielectric Matrix for All-Silicon Tandem Solar Cells. *Advances in OptoElectronics*.
- [11] Lan, H., & Ding, Y. (2012). Ordering, positioning and uniformity of quantum dot arrays. *Nano Today*, 7, 94-123.
- [12] Di, D, Perez-Wurfl, I, Conibeer, G, & Green, M. A. (2010). Formation and photoluminescence of Si quantum dots in SiO<sub>2</sub>/Si<sub>3</sub>N<sub>4</sub> hybrid matrix for all-Si tandem solar cells. *Solar Energy Materials & Solar Cells*, 94, 2238-2243.
- [13] Conibeer, G., Green, M., Corkish, R., Cho, Y., Cho, E., Jiang, C., Fangsuwannarak, T., Pink, E., Huang, Y., Puzzer, T., Trupke, T., Richards, B., Shalav, A., & Lin, K. (2006). Silicon nanostructures for third generation photovoltaic solar cells. *Thin Solid Films*, 511-512, 654-662.
- [14] Yastrebova, N. V. (2007). High-efficiency multi-junction solar cells: Current status and future potential. *Centre for Research in Photonics*.
- [15] Nychporuk, T., & Lemiti, M. (2011). Silicon-Based Third Generation Photovoltaics. In: Kosyachenko L.A. (ed.), *Solar Cells- Silicon Wafer-Based Technologies*, Rijeka: Intech, 139-176, Available from, <http://www.intechopen.com/books/solar-cells-silicon-wafer-based-technologies>, accessed 2 November 2011.
- [16] Green, M. A., & Conibeer, G. (2007). Nanostructured Silicon-Based Tandem Solar Cells. *PhD thesis. University of New South Wales, Sydney, Australia*.
- [17] Konig, D., Rudd, J., Green, M. A., & Conibeer, G. (2009). Impact of interface on the effective band gap of Si quantum dots. *Solar Energy Materials & Solar Cells*, 93, 753-758.
- [18] Pavesi, L., & Turan, R. (2010). Silicon Nanocrystals: Fundamentals, Synthesis and Applications. *Rijeka: WILEY-VCH Verlag GmbH & Co*.
- [19] Goodey, A. P., Eichfeld, S. M., Lew, K., Redwing, J. M., & Mallouk, T. E. (2007). Silicon Nanowire Array Photoelectrochemical Cells. *Journal of American Chemical Society*, 12912344-12345.

- [20] Huang, J., Hsiao, C., Syu, S., Chao, J., & Lin, C. (2009). Well-aligned single-crystalline silicon nanowire hybrid solar cells on glass. *Solar Energy Materials & Solar Cells*, 93, 621-624.
- [21] Zeng, L., Yu, X., Han, Y., & Yang, D. (2011). Performance of silicon nanowire solar cells with a phosphorus diffused emitter. *PhD thesis. Zhejiang University, Hangzhou, China.*
- [22] Garnett, E. C., & Yang, P. (2008). Silicon Nanowire Radial p-n Junction Solar Cells. *Journal of American Chemical Society*, 130, 9224-9225.
- [23] Syu, H., Shiu, S., & Lin, C. (2012). Silicon nanowire/organic hybrid solar cell with efficiency of 8.40%. *Solar Energy Materials & Solar Cells*, 98, 267-272.
- [24] Kuo, C. Y., Gau, C., & Dai, B. T. (2011). Photovoltaic characteristics of silicon nanowire arrays synthesized by vapor-liquid-solid process. *Solar Energy Materials & Solar Cells*, 95, 154-157.
- [25] Aliberti, P., Shrestha, S. K., Li, R., Green, M. A., & Conibeer, G. J. (2011). Single layer of silicon quantum dots in silicon oxide matrix: Investigation of forming gas hydrogenation on photoluminescence properties and study of the composition of silicon rich oxide layers. *Journal of Crystal Growth*, 32784-88.

